

The measurement of proton stopping power using proton-cone-beam computed tomography

Piotr Zygmanski^{†‡}, Kenneth P Gall^{§||}, Monroe S Z Rabin[†] and Stanley J Rosenthal[§]

[†] Department of Physics and Astronomy, University of Massachusetts, Amherst, MA 01003, USA
[§] Department of Radiation Oncology, Massachusetts General Hospital, Boston, MA 02114-2696, USA

Received 9 June 1999, in final form 2 September 1999

Abstract. A cone-beam computed tomography (CT) system utilizing a proton beam has been developed and tested. The cone beam is produced by scattering a 160 MeV proton beam with a modifier that results in a signal in the detector system, which decreases monotonically with depth in the medium. The detector system consists of a Gd₂O₂S:Tb intensifying screen viewed by a cooled CCD camera. The Feldkamp–Davis–Kress cone-beam reconstruction algorithm is applied to the projection data to obtain the CT voxel data representing proton stopping power. The system described is capable of reconstructing data over a 16 × 16 × 16 cm³ volume into 512 × 512 × 512 voxels. A spatial and contrast resolution phantom was scanned to determine the performance of the system. Spatial resolution is significantly degraded by multiple Coulomb scattering effects. Comparison of the reconstructed proton CT values with x-ray CT derived proton stopping powers shows that there may be some advantage to obtaining stopping powers directly with proton CT. The system described suggests a possible practical method of obtaining this measurement *in vivo*.

1. Introduction

Proton beam radiation therapy has been investigated in clinical applications for more than 40 years following the suggestion of Wilson (1946). Proton radiation therapy allows for superior dose conformation to a tumour target due to the physical properties of sharp lateral penumbra and the concentration of dose at the end of the proton range with no exit dose (Bragg peak). These properties make it possible to increase tumour target doses while reducing or maintaining dose levels to adjacent normal tissues. This may result in increased local control of some disease types (Munzenreider and Crowell 1994, Verhey and Munzenreider 1982).

The effective employment of protons in radiation therapy requires accurate knowledge of proton stopping power in three dimensions. This is traditionally obtained from an x-ray CT scan to which an empirically derived function is applied (Chu *et al* 1993, Hong *et al* 1996). The conversion of x-ray CT Hounsfield units to proton stopping powers is not exact since the dependence of x-ray attenuation on the Z and Z/A ratio of the material may differ significantly from the dependence of proton stopping power on these parameters. These systematic errors in

[‡] Present address: Department of Radiation Oncology, Massachusetts General Hospital, Boston, MA 02114-2696, USA.

^{||} Present address: Department of Radiation Oncology, University of Texas Southwestern Medical Center, Dallas, TX, USA.

calculation of the proton beam penetration depth result in the need to increase margins around a clinical target volume, thereby reducing the potential effectiveness of proton radiation therapy.

Schneider and colleagues reported results of extensive studies using proton radiographic techniques to examine the accuracy of current (heavy charged particle) proton treatment planning techniques (Schneider 1994, Schneider *et al* 1996). They conclude that due to incomplete modelling of multiple Coulomb scattering effects and the inaccuracy of proton stopping power derived from x-ray CT scans, significant deviations in predicted versus measured dose distribution could result. They reported inaccuracy in the measurement of the Hounsfield number to be up to a few per cent and found range differences of up to 1.5 cm for a 219 MeV proton beam.

Cormack's original interest in computed tomography was motivated in part by the problem of tissue inhomogeneity corrections needed for planning radiotherapy treatment. In his seminal papers on the application of x-ray absorption in radiology (Cormack 1963, 1964), Cormack pointed out the possibility of using heavy charged particles in the tomographic reconstruction. A number of early studies of heavy particle CT were carried out by Goitein (1972), Crowe and colleagues (Crowe *et al* 1975), Cormack and Koehler (1976), Hanson and colleagues (Hanson 1979, Hanson, *et al* 1978, 1981, 1982) and Holley and colleagues (Holley *et al* 1981). Cormack and Koehler addressed issues related to data artefacts in the projections near areas of sharp density inhomogeneities. Hanson and colleagues concluded that good density sensitivity could be achieved at up to about ten times lower cost in dose imparted to the patient than that for the x-ray techniques available at that time. In their work the scanned object was immersed in a water tank to avoid multiple Coulomb scattering (MCS) effects at low proton beam energies and to reduce the range in proton penetration over which the system needed to resolve.

All of these early investigations utilized data acquisition systems which used standard nuclear physics experimental techniques to gather CT projection data. This required recording individual events in which proton residual energy or range and in some cases particle track trajectory were recorded. Single event data acquisition rates limited the practicality of such systems for use with patients.

Motivated by these previous results, the system reported here was developed to investigate the possibility of measuring proton stopping power *in vivo* with sufficient accuracy and within reasonable data acquisition times to aid the process of treatment planning for proton radiation therapy. More specifically, the CT scanning system described here was developed to investigate the level of accuracy that might be practically achieved measuring proton stopping power directly with a proton CT system. Performing the CT scan with a cone beam, rather than the traditional CT fan beam geometry, significantly reduces the time required to obtain the projection data and increases spatial resolution in the cranio-caudal (superior–inferior) dimension. The technique of modulating the energy of the proton beam in such a way as to give a monotonically decreasing signal in the detector system versus depth of penetration of the beam further reduces the time required to obtain a single projection with sufficient signal. It is possible to imagine using such a system for *in vivo* measurements of proton stopping power.

2. Materials and methods

2.1. System overview

In order to measure the exit dose and from that obtain the water equivalent thickness (WET) or radiological thickness traversed by the proton ray, a cone-beam geometry was utilized rather than the traditional CT fan beam geometry. Additionally, in order to obtain proton penetration

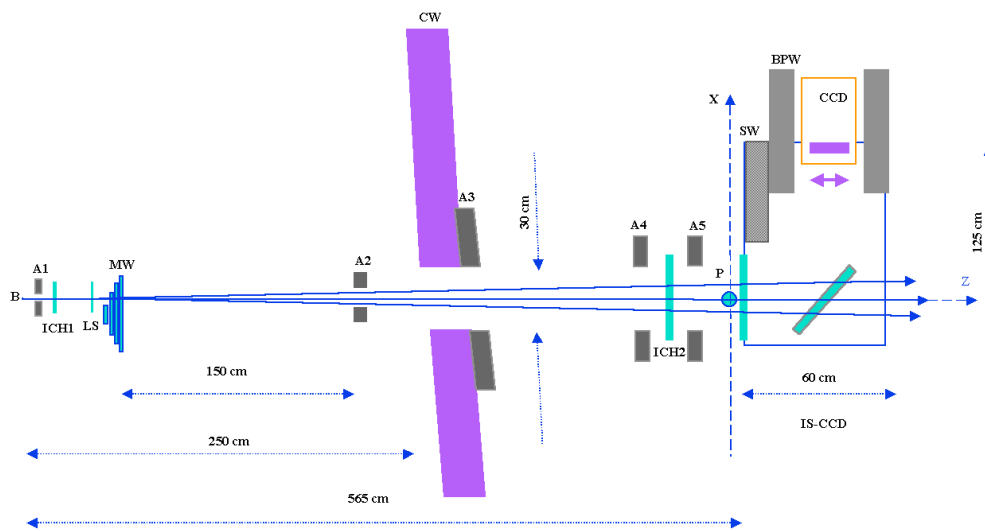


Figure 1. Elements of the PCB-CT beam line. The figure is drawn more or less to scale. The definitions of symbols are the following: B, monoenergetic proton pencil beam propagating along Z-axis; A1, A2, A3, A4, A5, apertures; ICH1, ICH2, ionization chambers; LS, lead scatterer; MW, linear modulating wheel; CW, thick concrete shielding wall; P, calibration phantom (a stack of PMMA plates of varying total thickness) or CT phantom (a PMMA cylinder containing resolution and contrast materials immersed in a water bath); IS-CCD, detector (intensifying screen-CCD camera system); SW, steel shielding wall; BPW, borated polyethylene shielding wall.

depth data without needing to measure individual proton events, we used a method, suggested by Koehler[†], of modulating the beam energy in such a way that a monotonically decreasing signal versus depth of penetration was produced in the detector system. A schematic drawing of the experimental set-up utilizing the Harvard Cyclotron Laboratory 158.6 MeV proton beam is shown in figure 1.

Figure 1 shows a scale drawing of the experimental geometry. The lead foil (LS)/modulator wheel (MW) were placed about 500 cm upstream of the centre of a rotating table on which the scanned object was placed (P). The front face of the detector system, housed in a light-tight box, was 10 cm downstream of the centre of rotation. Three collimators (A3, A4, A5) at approximately 100–200 cm upstream of the rotation centre of dimension about 30 cm limited the beam laterally while preserving adequate beam intensity over the useful imaging field. A parallel-plate ionization chamber (ICH2) upstream of the rotation centre served to monitor beam intensity and gate the beam for each projection exposure.

2.2. Beam energy modulator

The beam energy modulator (MW in figure 1) consists of four blades of variable thickness rotating about an axis parallel to the beam direction, with the thickness of each blade varying with angle. This method of modulating proton beam energy, in order to produce a uniform dose versus depth, was first reported by Koehler *et al* (1975) for downstream modulation. The method of using a modulator wheel far upstream, so that it could produce lateral scattering of the beam as well as uniform dose versus depth, was developed by Gottschalk and colleagues (Gottschalk *et al* 1991).

[†] The idea of the linear modulating was suggested by Andreas M Koehler in a private communication in 1994.

The beam energy modulator used for this work was designed using the techniques reported by Gottschalk but requiring a linearly decreasing signal versus depth. The wheel was machined from polymethylmethacrylate (PMMA). To provide for sufficient lateral scattering in regions of zero modulator wheel thickness, a 1 mm thickness of lead (LS) was placed immediately upstream of the wheel (MW).

Figure 2(a) schematically shows the formation of a linear response function of a perfect linear modulator. The modulating wheel used in the study was planned to produce a linear depth-dose curve; however, due to approximation errors in manufacturing made for reasons of practicality (influencing the accuracy but not the precision) the actual calibration curve showed variations from linearity. The experimental dose versus depth function, measured with an ionization chamber in a water tank and with a Gd₂O₂S:Tb screen-CCD system in PMMA, as well as the desired straight line response, are presented in figure 2(b). Calculated weights for variable thickness blades of the modulating wheel are included in figure 2(c).

The magnitude and character of deviations from linearity (figure 2(b)) depend on the penetration depth. For small depths (up to about 0.5 cm) a shoulder appears and this underestimates the ideal linear response by about 9% at $t = 0$ cm. This leads to errors in the CT reconstruction at the phantom edges, where MCS edge artefacts occur as well. The deviations from linearity in the middle of the curve are oscillations with a maximum amplitude of about 4%. These ambiguities in the calibration curve cause CT artefacts inside the phantom in certain areas and are of up to a few per cent (see section 3.1). The CT artefacts form visible patterns which can be identified easily by eye and their occurrence usually depends on location. The large peak at the end of the range is not of concern as it was beyond the greatest depth of penetration for the phantom used in this study. This peak at the end of the range, as well as the shoulder at its beginning and oscillations in the middle, can be eliminated with sufficient machining accuracy.

2.3. Detector system

A CCD camera (Photometrics) was used to record the light intensity produced in a Gd₂O₂S:Tb x-ray intensifying screen (Kodak, Lanex) by the modulated beam. The CCD camera utilized a Tektronix 512 × 512 pixel chip with square 27 μm pixels. It was cooled with a thermoelectric system to approximately -25 °C to reduce thermionic noise in the CCD during data acquisition. The CCD camera was optically coupled to the intensifying screen with an 85 mm focal length, $f/2.0$ lens (Nikkor). The camera was placed out of the direct proton beam by viewing the screen through a coated front surface mirror placed at a 45° angle.

The CCD camera was read out into a standard PC with a Pentium (Intel) CPU chip operating at 120 MHz. Data acquisition software was written in the PMIS language (Photometrics). The software allowed for triggered acquisition images recorded during a specified time interval, subtraction of bias and noise levels on a pixel by pixel basis, and normalization of signals in individual pixels to account for gain variations.

The detection efficiency versus dose deposited in the scanned object is almost entirely determined by the light output of the intensifying screen as a function of proton energy deposited in the object, the optical coupling efficiency of the CCD camera to the screen (determined by the f -number of the lens) and the quantum efficiency of detection of light photons of the CCD camera at the output wavelength of the intensifying screen (IS). No attempt was made to optimize the trade-offs in light collection efficiency versus image quality. Some of the elements of our system were matching those of Boon *et al* (1998). Their respective efficiencies were: (a) the scintillation efficiency (overall effectiveness of conversion of energy of electrons to visible light yield), 18%; (b) light escape (fraction of photons escaping the screen) of the

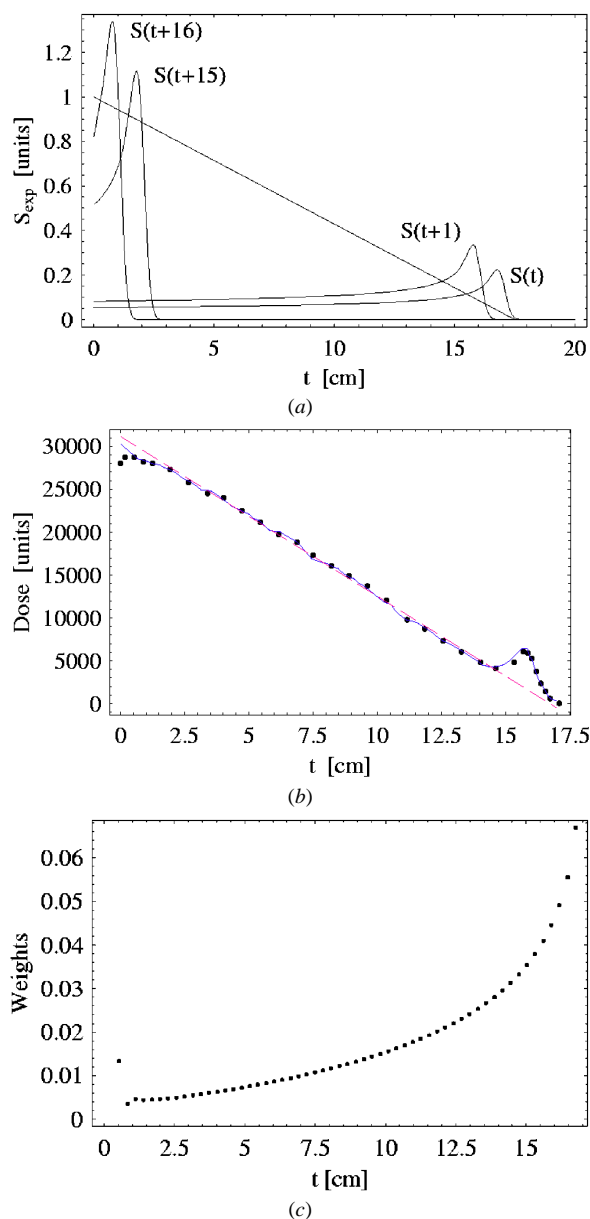


Figure 2. (a) Schematic representation of the construction of a linearly decreasing proton signal versus penetration depth. A series of Bragg curves (corresponding to different thicknesses of the wheel) are generated from a 158.6 MeV Bragg curve in water. The straight line dose is obtained by appropriately weighting and summing the individual Bragg curves. (The experimental Bragg curve data in water was provided by B Gottschalk at the HCL, Cambridge, USA.) (b) Comparison of calibration curves registered with the CCD and an ionization chamber in water. The beam was produced by the linear modulating wheel. The full curve is the dose in water along the beam axis measured by the ionization chamber immersed in the water tank. The water tank and the immersed ionization chamber replaced the CCD camera box (see figure 1) for this measurement. The points are the collective response of the whole CCD as a function of PMMA thickness (total dose to the intensifying screen in the area covered by the calibration images). The PMMA thickness is expressed in WET (water equivalent thickness) centimetres. (c) The PMMA weights calculated for the linear modulating wheel as a function of penetration depth for 158.6 MeV. The first weight is shifted because it accounts for the thickness of lead foil upstream of the PMMA wheel.

screen, 22%. We calculated the efficiency of the lens (the percentage of photons collected from the IS times the bulk transmission of the lens) to be 4% using the method described by Karellas *et al* (1992) and Radcliffe *et al* (1993). The quantum efficiency of the CCD chip at the dominant screen output wavelength of 545 nm was about 50% (data provided by the manufacturer, Photometrics).

In the current system image distortion was measured with a geometric grid and found to be negligible. Spatial resolution was limited by multiple Coulomb scattering (MCS) of protons before entering the detection system: typical values of ranges of MCS effects were from a few to 10 mm (in projection images), while the standard deviation of the narrow Gaussian of the point-spread-function (PSF) of the intensifying screen (IS) for protons is known to be about 1 mm (Boon *et al* 1998). The wide component of the Gaussian (glare) due to scattering within the screen and from the mirror was almost completely avoided and was negligible because of the large distance from the mirror to the IS and lack of PMMA phantom behind the screen (Heijmen *et al* 1995). Effects of veiling glare in a proton system similar to ours were investigated by Boon *et al* (1998). In order to make a clinical system these effects would have to be further investigated and minimized.

We did not try to measure the total detective quantum efficiency DQE of the intensifying screen–CCD camera system. However, we estimated DQE for our system to be about 0.002 at its zero spatial frequency (Boon *et al* 1998, Munro and Bouius 1998, Radcliffe *et al* 1993). We measured modulation transfer function (MTF) with the aid of the spatial resolution phantom described below. For reasons described in the previous paragraph, the MTF of the system basically reflects the amount of blurring introduced into the system by MCS effects (figure 3). The amount of MCS blur in the projection data varies with the total thickness of the phantom and phantom-to-screen distance. Should we wish to deconvolve the MCS blur from CT projections/reconstructions, we would have to address the issue of image blurring introduced by the IS–CCD camera system itself more carefully. Effects of this kind have been investigated for megavoltage x-ray portal imaging systems (Munro and Bouius 1998, Ruchala *et al* 1999).

The CCD detector was shielded from stray radiation in the experimental room that would produce excessive noise in the projection data. The predominant source of radiation noise is secondary neutrons produced by interactions of the proton beam in any of the materials it intersects. The proton beam was collimated to the useful imaging area with a series of collimators along the beam line to remove this source of neutrons from the detection system as far as practical. The CCD camera system was also surrounded by approximately 20 cm of borated polyethylene (BPW in figure 1) and in some areas 10 cm of steel (SW) to attenuate and stop the neutrons produced close to the detector system.

2.4. System calibration

The dose response of the detector system was calibrated as a function of beam penetration depth by placing various thicknesses of PMMA sheet at the approximate position of the scanning centre. This procedure allowed for normalization of the signal on an individual pixel basis, which also accounted for both the variation in proton beam intensity across the field and the variation in individual pixel gain factors.

Both the non-uniformities of the response of the IS and the non-flat profile of upstream proton beam fluence were accounted for in the calibration procedure, which used 2D + 1D data in a pixel by pixel fashion (2D across the field and 1D along the varying thickness of calibration phantom—a stack of PMMA plates).

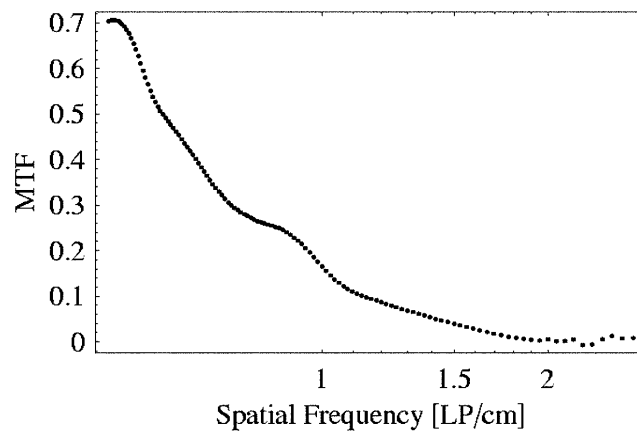


Figure 3. Modulation transfer function (MTF) measured with the aid of fan phantoms (see figure 4).

2.5. Phantom

A schematic diagram of the resolution and contrast phantom is shown in figure 4. The phantom was constructed to test the performance of the proton cone-beam CT (PCB-CT) system. The phantom was constructed from a 14 cm high PMMA tube of 9.5 cm diameter. Five different density materials were inserted into one 3 cm thick level. These materials were about 3 cm high and consisted of 2–2.5 cm diameter cylinders of air (trapped in a PMMA tube), vegetable oil, cork (inhomogenous) and plastic bone (RMI, Wisconsin).

At the middle plane of the phantom an arrangement of four thin PMMA wedges was inserted to provide spatial resolution information in the axial plane. At the lowest level of the phantom a similar arrangement of PMMA wedges was inserted to facilitate measurement of spatial resolution in the vertical plane. The remaining cylindrical volume of the phantom was then filled with water and sealed.

2.6. Data acquisition

Calibration data and projection data were obtained by manual triggering of a CCD camera exposure to coincide with the beam-on time. Exposures were made for 7 s while beam-on time was generally about 4 s. The total integrated beam signal recorded by the CCD as a function of the projection angle did not show any significant deviations from the average (for all angles), which implied that the beam was stable within the level of the photon noise. Projection data were taken of the phantom at 100 evenly spaced angles over a full rotation at 3.6° intervals. The phantom was rotated on a turntable manually between exposures. Rotation angle was measured with a physical scale on the turntable with an uncertainty of $\pm 0.5^\circ$.

At each angle two separate exposures were made. This was done in order to further process the images after acquisition and remove spurious noise that remained in the system from neutrons impinging on the CCD chip.

The relatively small number of views (100) and inaccuracies in the setting of the turntable were not a major concern. In general, undersampling the number of views in the CT projection data causes streak artefacts and inaccuracies in setting of the view angle, which leads to blurring of the CT image in the direction of the azimuthal angle (the larger the radius from the axis of rotation the larger the blurring). We have simulated these causes of CT artefacts and found them to be negligible compared with the MCS effects predominant in the real CT reconstructions.

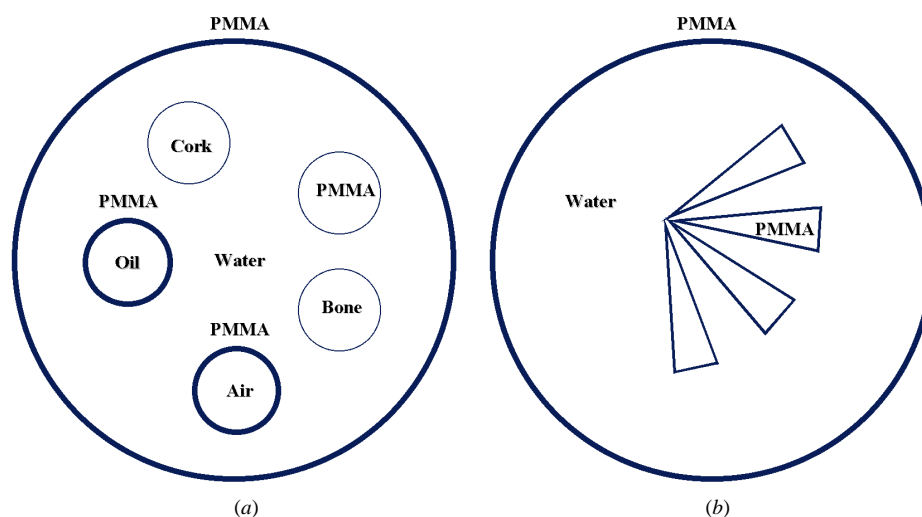


Figure 4. Horizontal cross sections through the contrast and resolution phantoms. The phantom is a PMMA cylinder filled with water and containing contrast (a) and resolution phantoms (b). The contrast phantoms are cylinders made of air, oil, cork, PMMA and artificial bone. Resolution phantoms are PMMA wedges forming two fans. One of the resolution phantoms measures resolution in the horizontal (b) and the other in the vertical plane (not shown).

In fact, the presence of MCS scattering in the projection data leads to cancellation of streak artefacts. Our study is a feasibility study. To develop a clinical proton cone-beam CT, we would need to collect many more views and use a precise turntable positioning system.

2.7. Total dose

The average total dose to the phantom (not dose per slice, but dose to the 3D volume) was estimated to be about 0.57 Gy for the 2×100 CT projections. This is equivalent to about 0.0026–0.0037 Gy per ray crossing the phantom in a single projection. The spread in dose arises from the fact that different parts of the phantom receive different doses. The surface gets more than deep-seated sites. The purpose of this study was to examine the feasibility of a practical proton cone-beam CT system using the available technological resources (as of 1997). We did not attempt to limit the relatively large dose per voxel. The poor overall efficiency of the optical system determined the number of protons contributing to a reconstructed voxel.

Efficiency of the IS-CCD camera system could be improved by a factor of approximately 500. Improvements in the efficiency of the system for a given CCD camera can be achieved primarily by using a faster lens and intensifying screen. The lens used in the experiments had an f -number of 2.0. A lens with an f -number of 0.95 would produce a gain factor of 4.4. In addition, one may use a faster intensifying screen. Recently studied Rarex PFG (ZnCdS:Ag) screens are 17 times faster than commonly used Lanex screens (Blackmore and Rynevald 1998). The CCD used in the experiment had a quantum efficiency at the level of 50%. A backed-thinned coated CCD had an efficiency up to 1.6 times as great. Also the CCD size may be increased to, for instance, $3 \text{ cm} \times 3 \text{ cm}$, which brings about another gain factor of 4.2. Larger CCD size implies larger magnification. When taken together, all the potential improvements listed would give a total gain factor of about 500.

A further considerable improvement of a proton cone-beam CT scanner may come from replacing the IS-CCD system with the recently developed large-area flat-panel array system

(Antonuk *et al* 1993, Munro and Bouius 1998, Yaffe and Rowlands 1997) (at the time of this study flat-panel devices were not available). The advantage of using a flat-panel device in proton cone-beam CT comes from the fact that this technique does not require lens coupling between the IS and CCD at all; CT projections are registered directly at the measuring plane with higher detection efficiency, higher resolution and within a very compact and even more practical design. All the major conclusions of this paper related to the MCS effects and their implications for the detection proton stopping power remain unchanged if one uses flat-panel devices in a proton scanner. Issues of radiation damage to these devices would need to be addressed.

2.8. Neutron noise

Neutron shields surrounding the CCD were not thick enough to stop all the secondary neutrons. This led to the appearance of neutron noise in the CT projection data. Neutron noise initially causes high signal in a cluster of pixels and after the charge is collected from the CCD pixels, makes them partially inactive during subsequent image acquisitions (i.e. their charge collection efficiency changes for a period). Most of the pixels recover after many image acquisitions, but a few do not and become permanently bad pixels. Correction of neutron noise was accomplished by comparing two projection images (for a given projection angle) or two calibration images (for a given thickness of calibration phantom) and correcting intensities of those pixels or pixel clusters that showed abnormally high deviations from local average intensity. This method corrected only part of the noise (the method that we used to find bad pixels was only sensitive above a certain threshold of about 10% from local average intensity). The remaining noise manifested itself in the reconstructions as circular artefacts. The circular artefacts were almost entirely corrected with a subtraction technique described below. Other sources of circular artefacts appearing in the reconstructions were treated in the same way as neutron noise generated circular artefacts.

After the initial reconstruction, circular artefacts remained due to uncorrected noise in the CCD pixels. This is probably the result of longer-term changes in the response of the CCD pixels after neutrons have interacted in them, and which are not accounted for in the pre-reconstruction processing.

To remove these artefacts, an average projection was constructed by summing projections over all angles. The CT image reconstructed from these projections showed the effects of the neutron noise as the circular artefacts. The average projection was then smoothed with a Gaussian filter and the resulting projection image was subtracted from the original average projection. The CT reconstruction from this projection showed only the circular artefacts. This circular artefacts reconstruction image was then subtracted from all original data reconstructions to remove the circular artefacts in them. At the central axis of rotation of the phantom, circular artefacts were not well corrected with this method. No further attempt was made to improve the images after this procedure.

2.9. Correction of MCS edge effects

The signal at a particular position of the detector contains information not only about energy loss along the ray, but also about the energy losses along adjacent rays from which protons have been scattered. The magnitude of these multiple Coulomb scattering (MCS) effects is dependent on detector position and the orientation of the phantom. These effects can be interpreted as shift- and angle-variant superposition. To the extent that these MCS effects distort the projections, the data do not completely satisfy the mathematical requirements on which the standard CT

reconstruction algorithms are based (in the sense that success of good CT reconstruction relies on consistent input data, a CT reconstruction algorithm can take corrupted data but what it calculates may be an untrue reconstruction). In our CT reconstruction we are using the Feldkamp–Davis–Kress (FDK) cone-beam CT reconstruction algorithm (Feldkamp *et al* 1984), which is known to be an approximation for the reconstruction planes not covering the source orbit. However, due to the fact that our cone beam has a very small cone angle (because of the large source–orbit radius) the approximations made in FDK algorithm are reliable (Webb *et al* 1987). The final effect is to degrade the spatial resolution of the reconstructions in many areas inside the reconstruction volume which leads to edge artefacts on the surface of the phantom, an area of sharp material inhomogeneity.

We were able to partially correct the MCS edge effects occurring in the projection data at the scanned object–air interface by applying a technique, described below, consisting of a redistribution of dose from the external to the internal region. The redistribution of dose was made in such a way as to conserve the overall area under the dose distribution. In this technique the localization of the artefacts in the image can be easily done by filtering the image with gradient filters. As a consequence, no information about the phantom geometry (location of the surface in the image) is needed. We used this technique for a cylindrical phantom, however, it can be straightforwardly extended to more complex geometries (patient skull for instance). The method relies on the severity of the MCS edge artefacts which take the form of sharp positive and negative spikes.

Figure 5 represents intensity measured in the x -direction (see figure 6). The edge of the phantom material occurs at a value of w_0 pixels (material is in the beam for all values of $w \geq w_0$), I_0 is the intensity for no material in the beam (open beam), I is the intensity measured with material in the beam and I_1 is the corrected intensity. Correction of the MCS edge effects consists of: (a) equating the projection signal $I(w)$ to the open-beam signal $I_0(w)$ in the region outside of the object; (b) subtracting the open-beam signal $I_0(w)$ from the original projection signal $I(w)$ and calculating an excess signal in the external region $\sum_{w < w_0} (I(w) - I_0(w))$; and (c) adding portions of the excess signal in the external region to the original projection signal $I(w)$ in the internal region in a power-law fashion $A(w - w_0)^n$. Parameters A and n are constants determined so that, starting from the edge and proceeding to the right, continuity of the resulting corrected signal $I_1(w)$ is achieved at the edge ($I_0(w_0^-) = I_1(w_0^+)$) and inside the phantom at a given position $w_1 > w_0$ ($I_1(w_1) = I(w_1)$).

It was necessary to perform this projection image correction in order to produce accurate proton stopping powers in the final reconstructed images. In section 3 we show that the proton stopping powers which were obtained with uncorrected projection images resulted in underestimated stopping powers everywhere inside the reconstructed images of the phantom. Simulations of the proton CT system led to our adoption of this method (Zygmanski 1998).

2.10. Reconstruction

After being recorded and calibrated, the projection data represent water equivalent thickness (WET) of the phantom as a function of position in the detector plane (u, v) (figure 6), which in turn represents an effective path integral of the stopping power ratio of protons $L(u, v, \gamma)$. The stopping power ratio of protons, $\eta(x)$, is a ratio of average (macroscopic) energy deposition per unit pathlength for a given material $S(x)$ to that for a reference material (water), $S_{\text{H}_2\text{O}}$

$$\eta(x) = \frac{S(x)}{S_{\text{H}_2\text{O}}} \Big|_{E(x)} \quad (1)$$

where the dependence on the location x within the material (which can be inhomogenous) is shown and both stopping powers are evaluated at the same energy, $E(x)$. Although the

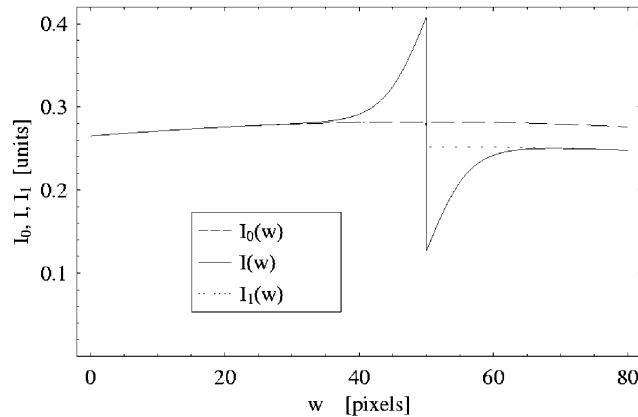


Figure 5. Schematic representation of the technique of correction of MCS edge effects occurring at the object edges. The left edge of the object is at $w_0 = 0.5$ and the right edge is not visible.

stopping power $S(x)$ is a function of energy, the stopping power ratio $\eta(x)$ is to a very good approximation for materials of interest (tissues) energy independent (Janni 1982). For high- Z materials, like steel or lead, η significantly depends upon energy. Thus we assume that the stopping power ratio is independent of proton energy and that spatial correlations due primarily to the MCS can be neglected. The path integrals $L(u, v, \gamma)$, from which the stopping power ratio is reconstructed, are along individual rays of the cone-beam for a given rotation angle, γ , of the source. The CCD pixels are at positions defined by a unit vector $\hat{n}(u, v)$ pointing from the beam source to coordinates (u, v) in the U - V plane

$$L(u, v, \gamma) = \int_0^\infty \eta(\mathbf{U}_\gamma \cdot \mathbf{x}(u, v, t)) dt. \quad (2)$$

Here, t is penetration distance in the direction of $\hat{n}(u, v)$, \mathbf{U}_γ is a rotation operator of the object coordinates representing rotation of the source by an angle γ

$$\mathbf{U}_\gamma = \begin{pmatrix} \cos(\gamma) & 0 & -\sin(\gamma) \\ 0 & 1 & 0 \\ \sin(\gamma) & 0 & \cos(\gamma) \end{pmatrix} \quad (3)$$

and $\mathbf{U}_\gamma \cdot \mathbf{x}$ is a position in the phantom coordinate system after rotation of the phantom by the angle γ . The integration is carried out along a path starting from a point, \bar{x}_0 , where the ray intersects the surface (figure 6) and proceeds in the direction of $\hat{n}(u, v)$

$$\mathbf{x}(u, v, t) = \mathbf{x}_0(u, v) + t\hat{n}(u, v). \quad (4)$$

The Feldkamp–Davis–Kress algorithm (FDK) (Feldkamp *et al* 1984) of reconstruction from the cone-beam projection data was adopted. The FDK algorithm is an extension of the fan-beam backprojection algorithm from 2D to the third dimension. It works well, although it assumes a set of projection data that do not satisfy Tuy's condition (Yan and Leahy 1991). Tuy's condition (Tuy 1983) states that the data are complete if and only if the source orbit is such that every plane intersecting the reconstructed object intersects the source orbit at least once. The FDK source orbit is a single circle, and as such, it does not completely fulfil conditions for exact inversion. However, the strict conditions imposed by the inversion formula can be relaxed in cases when the cone-beam angle is small (for this PCB-CT investigation the maximum cone angle is about 0.04 rad). The FDK algorithm is the only efficient and practical technique of reconstruction from cone-beam data known at present (Noo *et al* 1996).

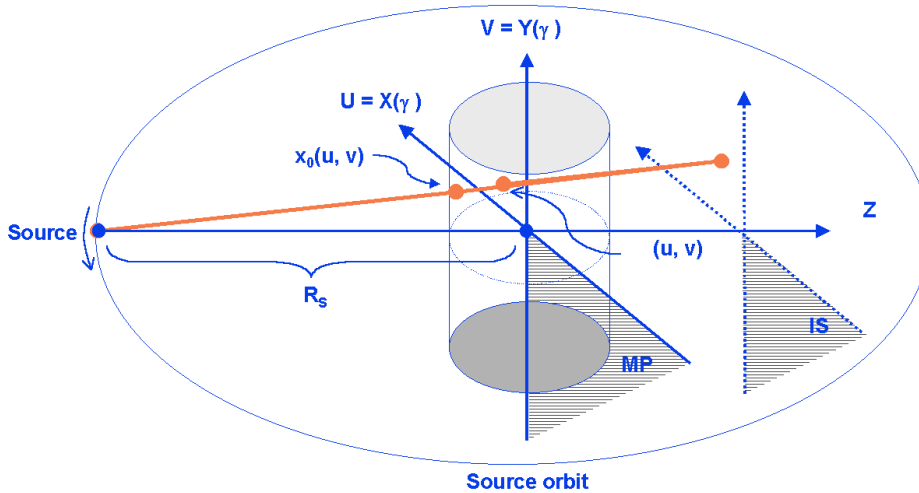


Figure 6. Cone-beam CT reconstruction geometry. Definition of the symbols: MP, measuring plane of the cone-beam CT algorithm; IS, intensifying screen (the true measuring plane); U - V , plane, including the axis of rotation, onto which the measured data are demagnified (In the reconstruction, we assume that the beam source and detection plane IS rotate about the rotation axis of the phantom. Experimentally, the beam source and IS are fixed and the phantom rotates about a vertical axis.); X - Y - Z , the proton beam coordinate system (For rotation angle $\gamma = 0$ the X - Y plane is equivalent to the U - V plane.); R_s , the source orbit radius (the distance from the effective source of radiation to the axis of rotation of the turntable). The CB-CT source orbit is a circle lying in the X - Z plane with its centre at the axis of rotation. $x_0(u, v)$ is the point of intersection of a proton ray with the upstream surface of the phantom.

The process of reconstructing a given slice in a plane perpendicular to the axis of rotation reduces to convolving the projection data along a number of rows in a given projection (up to seven rows in our experimental geometry) and then summing the result over all the projection angles. The FDK reconstruction algorithm, like other convolution backprojection algorithms, has to deal with the problem of performing reconstruction from incomplete data by application of a reconstruction kernel which vanishes beyond a certain cut-off frequency. For instance, in our study we have used only 100 projection angles, which makes the CT data not only discrete but also undersampled.

The convolution kernel we used in the algorithm was derived in a fashion similar to Webb (1982). It differs from the standard kernel used in cone-beam reconstruction, and is given by

$$g(u) = \left\{ \alpha \frac{1 - \cos(\bar{\omega}_0 \beta u)}{u} + (1 - \alpha) \frac{u(1 + \cos(\bar{\omega}_0 \beta u))}{u^2 - \beta^{-2}} \right\}_{u-\Delta u/2}^{u+\Delta u/2} \quad (5)$$

in which u is the position along a row, $\Delta u (=1)$ is the CCD detector size, $\bar{\omega}_0$ is the cut-off frequency, equal to $\pi/\Delta u$, and (α, β) are parameters controlling the amount of noise cancellation in the reconstruction. By a proper choice of kernel parameters α and β one can cancel statistical noise in the CT reconstructions, compromising the spatial resolution at the same time (Webb 1982). We chose parameters that partially cancel the noise while still having little impact compared with MCS effects, and preserve the average values of the reconstructed proton stopping power ($\alpha \approx 0.5$ and $\beta \approx 1.0$ – 1.7). When $\alpha = 0.5$ and $\beta = 1$ the kernel reduces to the Shepp–Logan filter (Shepp and Logan 1974). When $\beta < 1$ then details in the reconstruction are removed and when $\beta > 1$ they are enhanced compared with the standard filtering.

2.11. X-ray CT scan and Faraday cup measurements

An x-ray CT scan of the phantom was done with a conventional scanner (GE 9800) and the values of the corresponding proton stopping power ratios were calculated using an empirically derived function used in clinical practice at MGH (Mustafa and Jackson 1983) and described recently by Schneider *et al* (1996). The function can be described by a simple formula $\eta(H) = H/1000$ if $H < 40$, otherwise $((H - 40)/2 + 40)/1000$, where H is the Hounsfield number. The latter function is fit by a cubic spline function over H versus η data pairs: $\{(0, 0), \{800, 0.80\}, \{900, 0.95\}, \{1025, 1.025\}, \{1075, 1.075\}, \{1137.5, 1.0875\}, \{2500, 1.7333\}\}$.

An additional, independent measurement of stopping power was performed using a multi-layer Faraday cup[†] in the proton beam. This multi-layer Faraday-cup consists of a stacked array of Cu plates insulated from each other. With this detector, residual proton ranges can be determined with a precision of about ± 0.1 mm. Thicknesses of PMMA, artificial bone and vegetable oil were placed in the beam and their effect on the residual range of the beam was used to derive their stopping power.

3. Results

3.1. Reconstructed stopping power ratios

From the proton cone-beam CT (PCB-CT) reconstructions (figure 7) we took the value of the proton stopping power ratio in the central region of each of the contrast phantom materials. The value of the proton stopping power near the edge of the material was degraded (under-/over-estimated) by MCS effects. From simulations, we know that the correction technique (redistribution of dose at the phantom edges in projection images) described above reduced the magnitude of MCS edge effects at the air-phantom interface considerably (from about 200% to 25%) and decreased their impact on the phantom interior to a level below the statistical noise present in the reconstructions (Zygmanski 1998).

Table 1 summarizes the results. It can be seen that CT reconstructed values for PMMA and vegetable oil are in good agreement with the values obtained with a multilayer Faraday cup. The values for artificial bone and air are under- and over-estimated respectively. This is in accordance (both qualitatively and quantitatively) with the proton CT simulations, which show that for an inhomogeneity sufficiently dense/soft and small in size a 'leakage' of density from high- to low-density regions will occur. For the materials studied, the values of the stopping power ratio measured by the PCB-CT system are slightly better than those derived from the x-ray CT. This could be suspected based on the known differences in interaction between protons and photons. We predict that in general a proton scan will give a better agreement with reality than an x-ray scan in the areas that are not MCS limited.

The uncertainties listed for protons in table 1 represent only statistical variations (standard deviations) of reconstructed stopping power η in areas away from CT artefacts arising from calibration ambiguities. The uncertainties for x-rays also represent only statistical fluctuations in the CT images. Systematic uncertainties for x-rays arising from calibrations etc are not given; however, it is known that they may be up to a few per cent or even greater (Schneider *et al* 1996).

The uncertainties in η for proton CT are high because of residual neutron noise and low proton statistics. Proton statistics can be straightforwardly improved, as previously described

[†] The multi-layer Faraday-cup was developed by Bernard Gottschalk at the HCL, Cambridge, MA, USA.

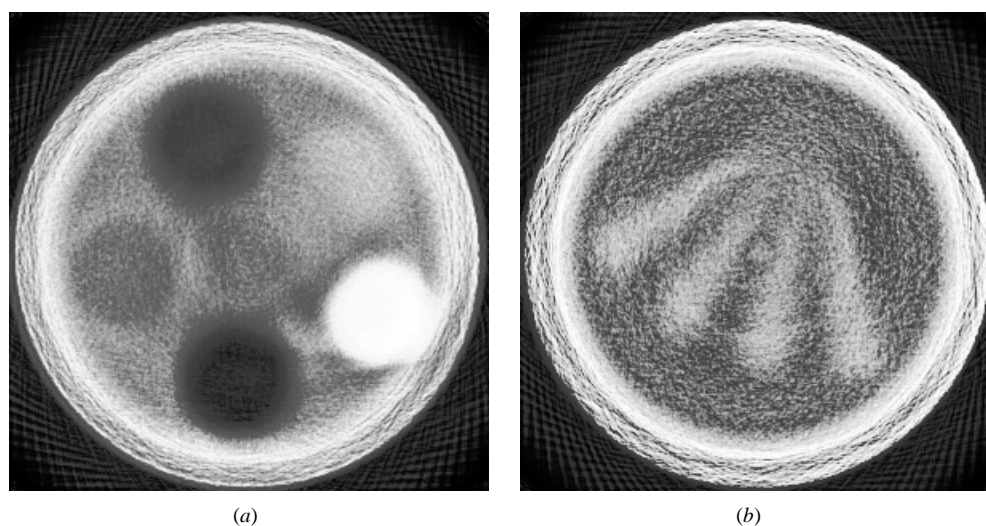


Figure 7. Experimental reconstruction of the contrast (a) and resolution (b) phantoms in the horizontal plane. The reconstructions are performed from the experimental projections calibrated by linearly interpolating between the calibration data points in figure 2(b). The raw projections were corrected for the neutron noise and MCS edge effects prior to, and the circular artefacts after, the reconstruction. The reconstruction kernel parameters used were $\alpha = 0.54$ and $\beta = 1.7$. Corresponding x-ray CT reconstructions are shown in figure 9.

Table 1. Table of proton stopping power ratios for different contrast phantoms in the areas far from the edges. X-ray CT stopping powers were calculated with two schemes based on data by Mustafa and Jackson (1983) (CT[†]) and Schneider *et al* (1996) (CT[‡]) respectively. Values from ICRU 49 are known only for air and PMMA (values averaged for 10, 50, 100, 200 MeV).

Material	PCB-CT	X-ray CT [†]	X-ray CT [‡]	ICRU 49	Faraday cup
Water	1.00 ± 4%	0.99 ± 0.3%	1.00 ± 0.3%	—	—
PMMA	1.17 ± 3%	1.08 ± 0.3%	1.08 ± 0.3%	1.16	1.17 ± 0.4%
Air	0.095 ± 47%	0.014 ± 0.3%	0.014 ± 0.3%	0.001	—
Artificial bone	1.59 ± 2%	1.78 ± 1%	1.74 ± 1%	—	1.67 ± 0.2%
Vegetable oil	0.95 ± 4%	0.88 ± 0.3%	0.92 ± 0.3%	—	0.97 ± 1.7%

in section 2.7. In addition, ambiguities in the calibration curve leading to artefacts in some areas of the images can be easily overcome by improved manufacturing of the modulating wheel. Once these sources of errors are diminished, effects of the neutron noise can be further analysed and possibly diminished as well.

3.2. Spatial resolution

Spatial resolution of the system was measured in both the axial and a vertical plane with the PMMA resolution fans inserted in the phantom (figures 7(b), 8 and 9(b)). The fan phantoms enabled us to evaluate the MTF of the system. As stated before, the MTF of the system is dominated by MCS blurring effects. In analysing the MTF signal as a function of fan line thicknesses one has to distinguish between the bare visual contrast of high versus low signals (PMMA fans versus water background) and a contrast that gives accurate values of stopping powers (uncorrupted by MCS). We estimate that the contribution to the blur from the imaging system (excluding MCS effects in the phantom) is a few per cent of the total blur. In

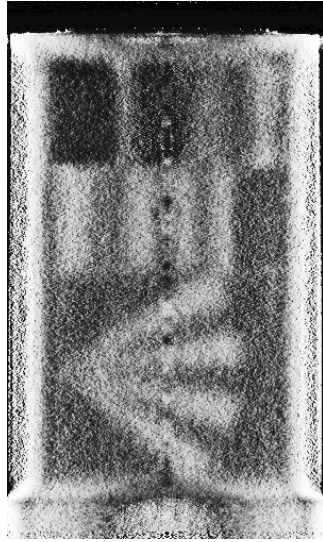


Figure 8. Experimental reconstruction of the whole phantom in the vertical plane. See caption to figure 7 for details.

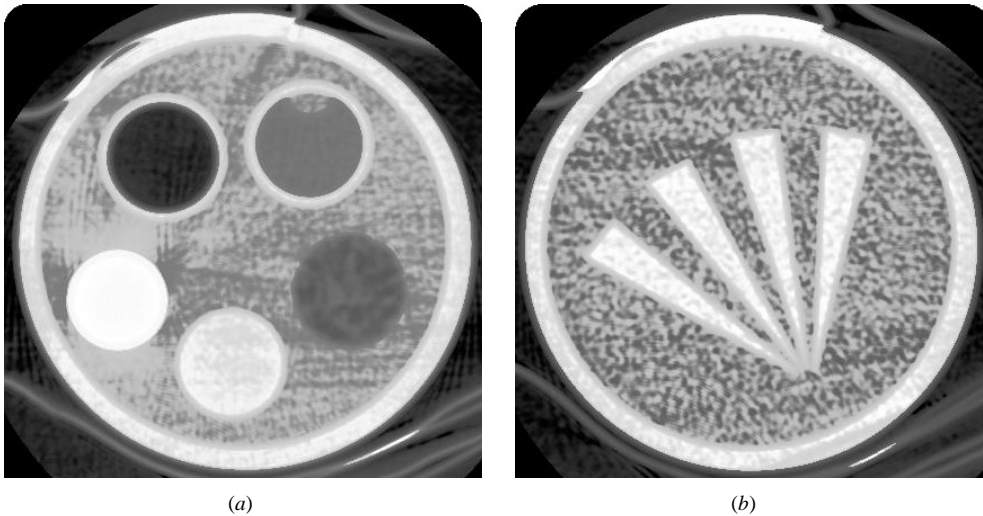


Figure 9. Two CT reconstructions obtained with the aid of an x-ray (GE 9800) scanner corresponding to proton reconstructions from figure 7. Contrary to proton CT reconstructions, the x-ray CT images were obtained for an optimal number of views and number of x-rays per view.

conventional diagnostic CT it is often of interest to determine at what limiting frequency one can visibly distinguish a given difference in density (bare visual contrast). However, for our purpose, we are interested in determining at what frequency the reconstructed proton stopping power deviates significantly from its true value. This, of course, occurs at a much lower spatial frequency.

The resolutions in the horizontal and vertical planes are virtually the same for the proton CT, while for x-ray CT the resolution in the vertical plane is limited by the slice thickness

(typically 3 mm, although smaller slices of 1 mm are possible). The spatial resolution at which reconstructed proton stopping powers are uncorrupted by the MCS effects is approximately 0.5 line pairs (lp) cm^{-1} . Visual contrast between the PMMA/water sections persists up to a limiting frequency of about 2 lp cm^{-1} for protons, and up to 10 lp cm^{-1} for x-ray CT (in the horizontal plane).

The data collected for the reconstruction were not optimized for spatial and contrast resolution as a function of signal strength. However, we do not expect improvements with increased number of protons per voxel to be appreciable due to the fact that the spatial resolution in the current proton CT reconstructions is mainly MCS- and not dose-limited. Improvements of spatial resolution with increased dose for the PCB-CT would become a consideration if we attempted to deconvolve the MCS blur from the CT reconstructions. However, this was not the goal of our study.

One advantage of the cone-beam system is the ability to achieve equally good spatial resolution in the vertical and axial planes. The corresponding disadvantage is that scatter in the object contributes to signal degradation across axial slices as opposed to the situation in a fan beam geometry where scatter out of the fan is not detected.

4. Conclusions

The proton-cone-beam computed tomography system described can be used to obtain proton stopping power directly. For the materials studied the values obtained for proton stopping power are in better agreement with directly measured values than the values arrived at in the conventional fashion by converting x-ray CT Hounsfield units once the effects of MCS blur have been taken into account. Computer simulations presented elsewhere (Zygmanski 1998) show that MCS blur effects may cause under- (for materials like bone) or over- (air) estimation of stopping powers. The amount of over- and under-estimation from experimental data that were not corrected for the MCS blur effects is consistent with theoretical predictions.

The spatial resolution of the PCB-CT system is limited by multiple Coulomb scattering effects. It is not possible to employ the strategies of partially correcting for MCS effects proposed by others for single-particle-detection systems (Schneider 1994), because of the lack of knowledge of the proton angle hitting the detector plane (intensifying screen) in our system. It may be possible to use deconvolution techniques to remove, or at least improve, the original images so that the spatial resolution of the reconstructions is improved to a level comparable to the inherent spatial resolution of the current system. Methods of deconvolution which could be used for the improvement of CT reconstruction rely on iterative blind deconvolution CT reconstruction. Such methods have been used to deal with effects similar to MCS blur effects and have been proven by others to work (Frey and Tsui 1993, 1994). Performing a full correction of MCS effects (both edge and blur effects) in the projection images is beyond the scope of this paper. Based on our simulations of CT data and on the derived formulae for the CT projections, our partial correction of the projections could serve as a starting point for an iterative reconstruction in the deconvolution process (Zygmanski 1998).

This PCB-CT system can be envisioned as a clinical tool to obtain data that would aid proton treatment planning. Optimization of the dose efficiency of the system would render a system that would impart a dose to a patient comparable to that of an x-ray CT scan. With automation of the data acquisition system the data acquisition time could be reduced to a few minutes. Whether the effects of multiple Coulomb scattering could be reduced enough to render significantly useful final planning data has not been determined. Further investigation into this area is needed.

Acknowledgments

The authors wish to thank Michael Goitein, Alfred Smith and Philip Judy for useful discussions and invaluable advice, and Miles Wagner, Bernard Gottschalk and Andreas Koehler for experimental, technical and practical assistance. This work was supported in part by NCI grants no 5-PO1-CA21239-22.

References

- Antonuk L E, Yorkston J, Huang W, Boudry J and Morton E J 1993 Large-area flat-panel a-Si:H arrays for x-ray imaging *Proc. SPIE* **1896** 18–29
- Blackmore E W and Rynevald S C 1998 Measurement of proton beam dose profiles using a sensitive scintillation screen observed by a CCD camera *XXVIII PTCOG Meeting (15–17 April, Loma Linda, CA)*
- Boon S N, Van Luijk P, Schippers J M, Meertens H, Denis J M, Vynckier S, Medin J and Grusell E 1998 Fast 2D phantom dosimetry for scanning proton beams *Med. Phys.* **25** 464–75
- Chu W T, Ludewigt B A A and Renner T R 1993 Instrumentation for treatment of cancer using proton and light-ion beams *Rev. Sci. Instrum.* **64** 2005–2122
- Cormack A M 1963 Representation of a function by its line integrals with some radiological applications *J. Appl. Phys.* **34** 2722–7
- 1964 Representation of a function by its line integrals with some radiological applications II *J. Appl. Phys.* **35** 2908–13
- Cormack A M and Koehler A M 1976 Quantitative proton tomography: preliminary experiments *Phys. Med. Biol.* **21** 560–9
- Crowe K M, Budinger T F, Cahoon J L, Elischer V P, Huesman R H and Kanstein L L 1975 Axial scanning with 900 MeV alpha particles *IEEE Trans. Nucl. Sci.* **22** 1752–4
- Feldkamp L A, Davis L C and Kress J W 1984 Practical cone beam algorithm *J. Opt. Soc. Am. A* **1** 612–19
- Frey E C and Tsui B M W 1993 A practical method for incorporating scatter in a projector-backprojector for accurate scatter compensation in SPECT *IEEE Trans. Nucl. Sci.* **40** 1107–16
- 1994 Modelling the scatter response function in inhomogeneous scattering media for SPECT *IEEE Trans. Nucl. Sci.* **41** 1582–93
- Goitein M 1972 Three-dimensional density reconstruction from a series of two-dimensional projections *Nucl. Instrum. Methods* **101** 509–18
- Gottschalk B, Koehler A M, Sisterson J M and Wagner M S 1991 The case for passive beam spreading *Proc. Proton Therapy Workshop, PSI (1991)* pp 50–3
- Hanson K M 1979 Proton computed tomography: the application of protons to computed tomography *IEEE Trans. Nucl. Sci.* **26** 1635–40
- Hanson K M, Bradbury J N, Cannon T M, Hutson R L, Laubacher D B, Macek R, Paciotti M A, Sandford S A and Steward V W 1981 Proton computed tomography of human specimens *Phys. Med. Biol.* **26** 965–83
- Hanson K M, Bradbury J N, Cannon T M, Hutson R L, Laubacher D B, Macek R, Paciotti M A and Taylor C A 1978 The application of protons to computed tomography *IEEE Trans. Nucl. Sci.* **25** 657–60
- Hanson K M, Bradbury J N, Koeppel R A, Macek R, Machen D R, Morgado R, Paciotti M A and Taylor C A 1982 Computed tomography using proton energy loss *Phys. Med. Biol.* **27** 25–36
- Heijmen B J, Pasma K L, Kroonwijk M, Althof V G M, de Boer J C J, Visser A G and Huizenga H 1995 Portal dose measurement in radiotherapy using electronic imaging device (EPID) *Phys. Med. Biol.* **40** 1943–55
- Holley W R, Tobias C A, Fabrikant J I, Llacer J, Chu W T and Benton E V 1981 Computerized heavy-ion tomography *Proc. SPIE* **273** 283–93
- Hong L, Goitein M, Bucciolini M, Comiskey R, Gottschalk B, Rosenthal S, Serago C and Urie M 1996 A pencil beam algorithm for proton dose calculations *Phys. Med. Biol.* **41** 1305–30
- Janni J F 1982 Proton range-energy tables 1 keV–10 GeV *At. Data Nucl. Data Tables* **27** 147–339
- Karellas A, Harris L, Liu H, Davis M and D'Orsi J 1992 Charged-couple device detector: performance considerations and potential for small-field mammographic imaging applications *Med. Phys.* **10** 1015–23
- Koehler A M, Schneider R J and Sisterson J M 1975 Range modulators for proton and heavy ions *Nucl. Instrum. Methods* **131** 437–40
- Munro P and Bouius D C 1998 X-ray quantum limited portal imaging using amorphous silicon flat-panel arrays *Med. Phys.* **25** 689–702
- Munzenrider J E and Crowell C 1994 *Radiation Oncology Technology and Biology* ed P M Mauch and J S Loeffler (Philadelphia, PA: Saunders) p 34

- Mustafa A A and Jackson D F 1983 The relation between x-ray CT number and charged particle stopping powers and its significance for radiotherapy treatment planning *Phys. Med. Biol.* **28** 169–76
- Noo F, Defrise M, Clack R, Roney T J, White T A and Galbraith S G 1996 Stable and efficient shift-variant algorithm for circle-plus-lines orbits in cone beam CT *Proc. ICIP-96: 1996 Int. Conf. on Image Processing* ed P Delogne (Lausanne: IEEE) p 539–42
- Radcliffe T, Barnea G, Wowk B, Rajapakse R and Shalev S 1993 Monte Carlo optimization of metal/phosphor screens at megavoltage energies *Med. Phys.* **20** 1161–9
- Ruchala K, Olivera G H, Kapatoes J M, Schloesser E A and Mackie T R 1999 Megavoltage CT imaging using the incomplete data collected during modulated-treatment delivery *Med. Phys.* **26** 1064
- Schneider U 1994 Proton radiography: a tool for quality control in proton therapy *Doctoral Dissertation* No 10780 Universität Bayereuth, Spielberg, Germany
- Schneider U, Pedroni E and Lomax A 1996 The calibration of CT Hounsfield units for radiotherapy treatment planning *Phys. Med. Biol.* **41** 111–24
- Shepp L A and Logan B F 1974 The Fourier reconstruction of a head section *IEEE Trans. Nucl. Sci.* **21** 21–32
- Tuy H K 1983 An inversion formula for cone-beam reconstruction *SIAM J. Appl. Math.* **43** 546–52
- Verhey L J and Munzenrider J E 1982 Proton beam therapy *Ann. Rev. Biophys. Bioeng.* **11** 331–9
- Webb S 1982 A modified convolution reconstruction technique for divergent beams *Phys. Med. Biol.* **27** 419–23
- Webb S, Sutcliffe J, Burkinshaw L and Horsman A 1987 Tomographic reconstruction from experimentally obtained cone-beam projections *IEEE Trans. Med. Imaging* **6** 67–72
- Wilson R R 1946 Radiological use of fast protons *Radiology* **47** 331–9, 487–91
- Yaffe M J and Rowlands J A 1997 X-ray detectors for digital radiography *Phys. Med. Biol.* **42** 1–39
- Yan X and Leahy R M 1991 Derivation and analysis of a filtered backprojection algorithm for cone beam projection data *IEEE Trans. Med. Imaging* **10** 462–72
- Zygmanski P 1998 Proton-cone-beam-computed-tomography *PhD Dissertation* University of Massachusetts, Amherst